Journal of Materials Chemistry A

ROYAL SOCIETY OF CHEMISTRY

PAPER

View Article Online
View Journal | View Issue

Cite this: J. Mater. Chem. A, 2020, 8, 22075

Enabling stable MnO_2 matrix for aqueous zinc-ion battery cathodes†

Yiding Jiao, [a] Liqun Kang, [b] Jasper Berry-Gair,[a] Kit McColl, [a] Jianwei Li,[a] Haobo Dong,[a] Hao Jiang, [c] Ryan Wang, [b] Furio Corà, [a] Dan J. L. Brett, [b] Guanjie He *[abd] and Ivan P. Parkin *[a]

The primary issue faced by MnO_2 cathode materials for aqueous Zn-ion batteries (AZIBs) is the occurrence of structural transformations during cycling, resulting in unstable capacity output. Pre-intercalating closely bonded ions into the MnO_2 structures has been demonstrated as an effective approach to combat this. However, mechanisms of the pre-intercalation remain unclear. Herein, two distinct δ-MnO_2 ($K_{0.28}MnO_2 \cdot 0.1H_2O$ and $K_{0.21}MnO_2 \cdot 0.1H_2O$) are prepared with varying amounts of pre-intercalated K^+ and applied as cathodes for AZIBs. The as-prepared $K_{0.28}MnO_2 \cdot 0.1H_2O$ cathodes exhibit relatively high specific capacity (300 mA h g^{-1} at 100 mA g^{-1}), satisfactory rate performance (35% capacity recovery at 5 A g^{-1}) and competent cyclability (*ca.* 95% capacity retention after 1000 cycles at 2 A g^{-1}), while inferior cyclability and rate performance are observed in $K_{0.21}MnO_2 \cdot 0.1H_2O$. A stable δ-$MnO_2$ phase is observed upon cycling, with the reversible deposition of $Zn_4SO_4(OH)_6 \cdot 5H_2O$ (ZSH), ion migration between electrodes and synchronous transition of Mn valence states. This work firstly and systematically reveals the role of the pre-intercalated ions *via* density functional theory simulations and show that above a threshold K/Mn ratio of *ca.* 0.26, the K ions suppress structural transformations by stabilizing the δ phase. To demonstrate its commercial potential, AZIBs with high-loading active materials are fabricated, which deliver adequate energy and power densities compared with most commercial devices.

Received 2nd September 2020
Accepted 19th October 2020

DOI: 10.1039/d0ta08638j

rsc.li/materials-a

Introduction

Issues of energy shortage and environmental pollution need to be addressed for human survival and social development. Thus, the development of renewable energy sources such as solar, wind and hydropower has become a global imperative.[1,2] To effectively deliver energy from renewable sources and decarbonize transport systems, energy storage devices with desirable capacity, rate performance and cyclability are required. Li-ion batteries (LIBs) have been commercialized for portable devices and electric vehicles due to their wide operating voltage window and competitive energy/power densities.[3] However, safety issues, expensive configurations, and concerns about critical materials availability are barriers to future development and applications.[4–6] Therefore, cost-effective, safe, and environmentally-friendly energy storage devices as alternatives to LIBs are in urgent demand. Among other candidates, such as technologies based on alternate charge-carrying cations (*e.g.* K^+, Na^+, Al^{3+} and Ca^{2+}),[7–9] aqueous Zn-ion batteries (AZIBs) are drawing significant attention due to their low redox potential (−0.76 V *vs.* standard hydrogen electrode), outstanding theoretical capacity (820 mA h g^{-1}), abundant resources, high safety and ambient fabrication.[10–12]

Although extensive research focuses on Zn anodes and electrolyte modifications, a reliable and high-performance cathode has always been pursued to commercialize AZIBs. Among the candidates, vanadium-based cathodes exhibit the highest specific capacity (>300 mA h g^{-1}) and prolonged cyclability, but their working voltage window is relatively low (<1.0 V *vs.* Zn/Zn^{2+}), which hinders their practical use for high energy density applications.[13–17] Prussian blue analogs (PBAs) operate at a high working voltage (1.5–1.7 V *vs.* Zn/Zn^{2+}) but suffer from the relatively low specific capacity (50–120 mA h g^{-1}).[18,19] Manganese-based cathodes not only share outstanding specific capacity (200–300 mA h g^{-1}) and high working voltage range (1.3–1.35 V *vs.* Zn/Zn^{2+})[20–24] but also exhibit the advantages of abundant reserves, simple fabrication, low cost and environmental friendliness, and have therefore become a research

[a]Christopher Ingold Laboratory, Department of Chemistry, University College London, 20 Gordon Street, London WC1H 0AJ, UK. E-mail: g.he@ucl.ac.uk; i.p.parkin@ucl.ac.uk

[b]Department of Chemical Engineering, University College London, Torrington Place, London WC1E 7JE, UK

[c]Key Laboratory for Ultrafine Materials of Ministry of Education, Shanghai Engineering Research Center of Hierarchical Nanomaterials, School of Materials Science and Engineering, East China University of Science & Technology, 130 Meilong Road, Shanghai 200237, China

[d]Joseph Banks Laboratories, School of Chemistry, University of Lincoln, Green Lane, Lincoln, LN6 7DL, UK

† Electronic supplementary information (ESI) available. See DOI: 10.1039/d0ta08638j

hotspot.[25–27] However, the application of manganese-based cathodes is severely hindered by substantial intrinsic issues. The soluble Mn^{2+}, derived from the disproportionation reaction of Mn^{3+} and structural transformation, causes severe capacity decay upon cycling.[28–34] Structural transformations are likely to occur between the tunnel and layered structures.[30] According to previous reports, α-, β-, γ-, and λ-MnO_2 usually experience phase transition into Zn-buserite, during which the volumetric change associated with this process causes significant residual stress and contributes to the amorphized manganese-based cathodes, ultimately leading to capacity loss during cycling.[35] Several strategies have been proposed to improve performance. As an electrolyte additive, $MnSO_4$ has been proven to suppress excessive Zn^{2+} insertion by limiting Mn vacancies upon cycling and maintaining structural integrity.[36] The hybridization with carbon-based materials, such as graphene and carbon nanotubes, has been demonstrated as an efficient method to provide a protective host structure and prolongs the cyclability.[20,37–43]

Pre-intercalation has been widely applied in other layered materials such as vanadium oxides to enhance stability upon cycling; choice of the interlayer guest species acting as structure stabilizing "pillars" allows to tune lattice spacing, enhance ion mobility, confer inherent conductivity *via* shallow donor levels associated with reduced V ions.[38,44–48] Besides, the presence of interlayer water in aqueous batteries screens the interaction between intercalated ion and cathode, leading to faster intercalation processes. Likewise, pre-intercalation of closely bonded ions has also been preliminarily studied to improve the performance of Mn-based cathodes.[20] The effect of pre-intercalated ions is concluded as the electrostatic force between per-intercalated ions and O and the enhanced structural stability. However, such a conclusion is too vague and omits the possible structural transformation induced by the pre-intercalation, which leaves the working mechanism of pre-intercalation an unexplored area. The structure–performance relationship between pre-intercalated cations and electrochemical behavior needs to be considered and discussed.

In this work, two K^+ pre-intercalated birnessite MnO_2 materials with varied amounts of K^+ were prepared *via* sol–gel and hydrothermal methods, respectively. Detailed physical and electrochemical characterizations were executed to disclose their dissimilarities in composition and the impact on electrochemical behavior. The AZIBs fabricated with $K_{0.28}MnO_2 \cdot 0.1H_2O$ ($K_{0.28}$MO) deliver a relatively high specific capacity of 300 mA h g^{-1} at 100 mA g^{-1}. Even at a high current density of 2 A g^{-1}, the AZIBs exhibit a sufficient specific capacity of 100 mA h g^{-1} and maintain >95% of their capacity over 1000 cycles, which is at the top level of relevant materials.[26,27] In contrast, the AZIBs fabricated with $K_{0.21}MnO_2 \cdot 0.1H_2O$ ($K_{0.21}$MO) exhibit inferior performance. The energy storage mechanisms are thoroughly investigated with systematic *ex situ* analysis. A stable δ-MnO_2 primitive phase was observed throughout the cycling process, along with the reversible deposition/dissolution of $Zn_4SO_4(OH)_6 \cdot 5H_2O$ (ZSH) phase, ion migration and simultaneous change of Mn valence state. The pre-intercalated K ions's underlying function was further scrutinized *via* density functional theory (DFT) simulations, demonstrating the phase selection role played by the K/Mn ratio and thus the structural stabilization for the birnessite phase achieved *via* the pre-intercalation of K ions at higher concentration. Moreover, to demonstrate practical applications, batteries were assembled with high loading (*ca.* 10 mg cm^{-2}) of active materials, which show outstanding energy and power densities compared to current commercial energy storage systems.

Results and discussion

Materials and characterization

Birnessite $K_{0.28}$MO was synthesized with a sol–gel method, while birnessite $K_{0.21}$MO was obtained *via* a one-step hydrothermal process (detailed methods are described in ESI†). Transmission electron microscopy (TEM), X-ray fluorescence analysis (XRF), energy-dispersive X-ray spectroscopy (EDX) and coupled elemental mappings were used to characterize the morphology and elemental distribution.

$K_{0.28}$MO exhibits nanoplates's shape with a width and length of 50–100 nm (Fig. S1A†). The morphology of $K_{0.28}$MO and $K_{0.21}$MO are similar and further supported by the results shown in Fig. S2A, S1B, C and D.† Furthermore, the crystallographic structures of the two materials were studied by X-ray diffraction (XRD, Fig. 1A). All X-ray diffraction characteristic peaks of the two materials are perfectly indexed to the birnessite $K_{0.28}MnO_2 \cdot 0.54H_2O$ phase (hexagonal, $R\bar{3}m$ (166), JCPDS 86-0666).[49,50] The magnified image of the (003) diffraction peak shows that in $K_{0.28}$MO, it shifts towards higher diffraction angles compared with $K_{0.21}$MO.[28,51] The enlarged TEM image further reveals that the lattice spacing of $K_{0.28}$MO is 7.04 Å, which corresponds to the (003) lattice plane (Fig. S1B†). The homogenous elemental distribution of K, Mn and O is observed in $K_{0.28}$MO (Fig. S3†). XRF analysis proves that the molar K/Mn ratio of $K_{0.28}$MO is 0.28, while for $K_{0.21}$MO, the ratio is 0.21

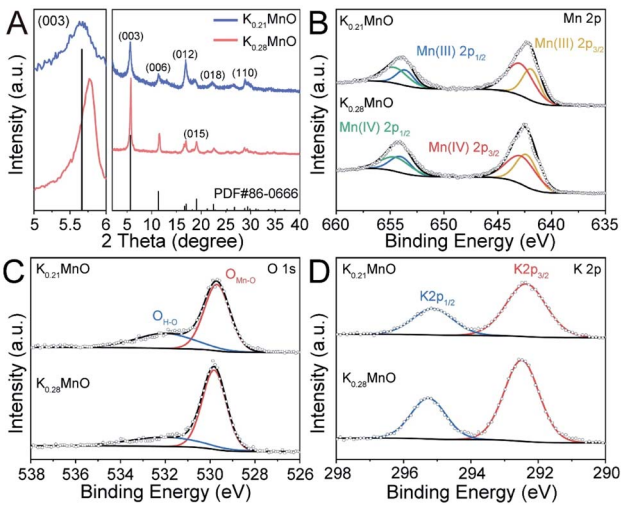

Fig. 1 Material Characterization. (A) XRD patterns of $K_{0.21}$MO and $K_{0.28}$MO. (B) Mn 2p XPS spectra of $K_{0.21}$MO and $K_{0.28}$MO. (C) O 1s XPS spectra of $K_{0.21}$MO and $K_{0.28}$MO. (D) K 2p XPS spectra of $K_{0.21}$MO and $K_{0.28}$MO.

(Fig. S2E and S1F†). The water contents of both materials were further investigated by thermogravimetric analysis (TGA), as shown in Fig. S4.† Most of the physically absorbed water content evaporates from room temperature to 150 °C. Complete loss of structural water content occurred between 150 °C and 500 °C. The removal of the structural water content corresponds to a 2 *wt*% loss of total mass, corresponding to 0.1 moles of H_2O per mole of $K_{0.28}MnO_2$ or $K_{0.21}MnO_2$.

To validate the counter-intuitive result that increased interlayer concentration of K causes a contraction of the interlayer separation, we performed a series of DFT calculations examining the equilibrium structure of K_xMnO_2 at varying K content x between 0 and 0.5. The results concerning the c lattice parameter and snapshots of the interlayer structures are reported in Fig. S5.† We observe an increase of interlayer spacing at low K content, followed by a contraction beyond a threshold value of *ca.* 0.3, which results from the stronger electrostatic interaction between the intercalated K^+ ions and the reduced MnO_2 layers. A contraction of interlayer separation, as observed experimentally, is therefore consistent with the atomic information provided by the computational study. The DFT-optimized lattice parameter for intercalant free δ-MnO_2 is 13.05 Å, which expands to 20.32 Å upon intercalation of water at an H_2O/Mn ratio of 0.25. Both values are in good agreement with experiment and previous reports.[52,53]

X-ray photoelectron spectroscopy (XPS) was applied to analyze the chemical composition and electronic structure of the two materials. As shown in Fig. 1B, both materials deliver similar Mn 2p shoulder peaks, which can be attributed to Mn $2p_{1/2}$ (654.4 eV) and Mn $2p_{3/2}$ (642.7 eV) with a spin-orbital splitting of 11.7 eV. A slight difference in the Mn(IV) and Mn(III) ratio is observed, deriving from different pre-intercalated K^+ concentrations. The presence of O and K can also be confirmed by O 1s and K 2p spectra. As shown in Fig. 1C, two characteristic peaks in the O 1s spectra can be identified as O_{Mn-O} (529.7 eV) and O_{H-O} (532.0 eV). Two shoulder peaks are also noted in the K 2p scan, which can be ascribed to K $2p_{1/2}$ (295.2 eV) and K $2p_{3/2}$ (292.5 eV) with the spin-orbital splitting of 2.77 eV (Fig. 1D).

Raman spectra are further applied to study the inter-layer and intra-layer bond strength (Fig. S6†). The Raman shift at *ca.* 640 cm^{-1} is assigned to the inter-layer Mn–O bonds, while the Raman shift at *ca.* 570 cm^{-1} is assigned to the intra-layer Mn–O bonds. It is indicated that the inter-layer Mn–O bonds have been strengthened in $K_{0.28}MnO$, while the intra-layer Mn–O bonds are weakened.

Further proof of the difference in Mn valence states in the bulk structures of these two materials can be found in the Mn $L_{3,2}$-edge near-edge X-ray absorption fine structure (NEXAFS spectra). As shown in Fig. S7A,† Mn $L_{3,2}$-edge absorption features for both materials are very similar but different from c-Mn_2O_3 and c-MnO standard reference samples. The intensity ratio of L_3/L_2 absorption of both materials shows similarities with β-MnO_2, which confirms high-spin states and similar oxidation states of Mn(IV). However, the first absorption peak at 641 eV is distinguished from the prominent absorption peak at 643.5 eV compared to β-MnO_2, which results from Mn's different chemical environments in the framework. In the magnified L_3-edge features, a slight shift (~0.2 eV) towards lower energy of both the leading-edge position and the gravity center of the L_3-edge is observed (Fig. S7B†), while similar shifts also exist in the L_2-edge (Fig. S7C†), which both indicate a lower Mn oxidation state in $K_{0.28}MO$ compared to $K_{0.21}MO$.

Electrochemical performance

The as-synthesized materials were assembled as cathodes in AZIB coin cell configurations using 3 M $ZnSO_4$ and 0.2 M $MnSO_4$ aqueous solution as the electrolyte for electrochemical tests. Fig. 2A illustrates the CV curves of $K_{0.28}MO$ at different scan rates from 0.1 to 1.0 mV s^{-1}. Two couples of redox peaks can be observed, indicating a two-step electrochemical process. With the increase of the scan rate, CV curves present minor peak shifts, representing dependable reversibility and stability during the polarization processes. A linear fitting was further carried out between peak current densities (i) and the square root of the scan rate ($v^{1/2}$) to evaluate the diffusion-controlled and capacitive contributions. It was calculated that the capacitive contribution is 53.7% of the total specific capacity at 0.1 mV s^{-1}, and it gradually increases to 78.6% at 1.0 mV s^{-1} (Fig. 2B). CV curves are also measured with $K_{0.21}MO$, which shows a similar two redox couple system and demonstrates similar electrochemical processes (Fig. S8A†). The capacitive contribution of $K_{0.21}MO$ is 34.7% at 0.1 mV s^{-1} and 62.7% at 1.0 mV s^{-1}, much lower than that of the $K_{0.28}MO$ cathode, which can be explained by more active surface charge storage of $K_{0.28}MO$ (Fig. S8B†). To further understand the inherent resistive behavior of both materials, EIS was performed before and after the cell was charged and discharged for 200 cycles at 2 A g^{-1}. We observed no change in charge-transfer resistance (R_3) of $K_{0.28}MO$, but there is an increase of R_3 for $K_{0.21}MO$ (Fig. S8C and D†).[2,54] It is reported that the dissolution of Mn is the primary reason for the capacity loss and impedance rise.[55] Therefore, the results indicate that a higher amount of pre-intercalated K^+ ions effectively suppress the Mn dissolution and subsequent impedance rise.

To further elucidate the dissimilarity in electrochemical performance resulting from pre-intercalation, cycling performance and charge/discharge profiles were measured in AZIB

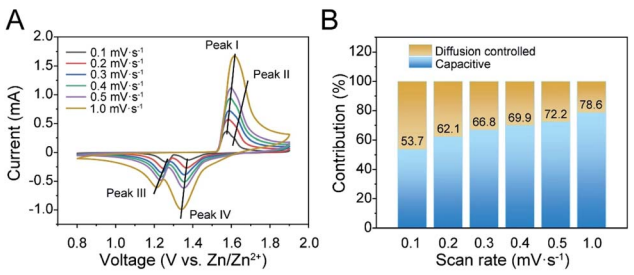

Fig. 2 Electrochemical behavior of $K_{0.28}MO$ in 3 M $ZnSO_4$ + 0.2 M $MnSO_4$ electrolyte. (A) Cyclic voltammetry (CV) curves of $K_{0.28}MO$ material at different scan rates from 0.1–1.0 mV s^{-1}. (B) The corresponding capacitive and diffusion-controlled contribution from the CV curves.

coin cells. As shown in Fig. 3A, at 100 mA g^{-1}, $K_{0.28}MO$ exhibited a lower initial capacity of 150 mA h g^{-1} with a gradual rise to 300 mA h g^{-1} at the 50th cycle. By contrast, $K_{0.21}MO$ exhibited a higher initial capacity of 230 mA h g^{-1}, while the capacity reached only 260 mA h g^{-1} at the 50th cycle. The comparison of low rate performance confirms that higher amounts of pre-intercalated K^+ help maintain structural integrity, ensuring a higher cycling capacity. However, the pre-intercalated K^+ ions occupy the active sites for Zn intercalation and thus hinder the intercalation/deintercalation of other cations in the first few cycles, sacrificing a part of the initial capacity. The cycle number was further extended to 60 to prove the cycling stability of $K_{0.28}MO$ at the low rate. The battery can maintain a specific capacity of >300 mA h g^{-1} after the 50th cycle (Fig. S9†).

The rate performance of both materials was further evaluated. Both materials exhibit good rate performance after 10 cycles of activation. The capacity retention at 5 A g^{-1} for the $K_{0.28}MO$ cathode is 35% of the value measured at 100 mA g^{-1} (Fig. 3B), while for $K_{0.21}MO$, the capacity retention is 28% (Fig. S10†). This can be explained by the better structural integrity upon cycling achieved in $K_{0.28}MO$. The charge/discharge profiles at the 1st, 10th, 20th, 30th, 40th and 50th cycles at the current density of 100 mA g^{-1} are reported in Fig. 3C and D. The typical two-stage voltage plateaus are fully retained after 50 cycles, illustrating the steady reaction kinetics.

To further confirm the cyclability at a high rate, both materials are cycled at 2 A g^{-1} for 1000 cycles (Fig. 3E). $K_{0.28}MO$ exhibited a high specific capacity of 100 mA h g^{-1} and high capacity retention of 95%, while for $K_{0.21}MO$, the specific capacity dropped rapidly with 30% decay. It is inferred that the higher concentration of K^+ ions helps to stabilize the layer structure and thus prevent the cathode from self-dissolution and amorphization upon cycling, which significantly prolongs the AZIB cycle life.

To further confirm the influence of K pre-intercalation. $K_{0.28}MO$ was further compared with pristine δ-MnO_2 with no pre-intercalated cations. As depicted in Fig. S11A,† the (003) interlayer spacing of δ-MnO_2 is larger than both $K_{0.28}MO$ and $K_{0.21}MO$, which derives from the repulsive force between the interlayer O atoms. EDX analysis further confirms pure Mn and O elemental distribution with no pre-intercalation (Fig. S11B†).

The CV analysis also shows two couples of redox peaks and a two-step reaction process. However, the peak current and position slightly differ from $K_{0.28}MO$, which results from the difference in the chemical environment and the subsequent difference in reaction kinetics (Fig. S12†).

As a consequence, the cycling stability of δ-MnO_2 demonstrates results consistent with expectations. Specifically, as shown in Fig. S13,† the maximum capacity reaches 150 mA h g^{-1}, which is much higher than $K_{0.28}MO$, demonstrating outstanding energy storage capability of the δ-MnO_2 phase. However, the specific capacity of δ-MnO_2 experienced a fast decline of more than 1/3 of its maximum capacity. The cycling instability comes from the unsupported unstable δ-MnO_2 and subsequent dissolution of the cathode material.

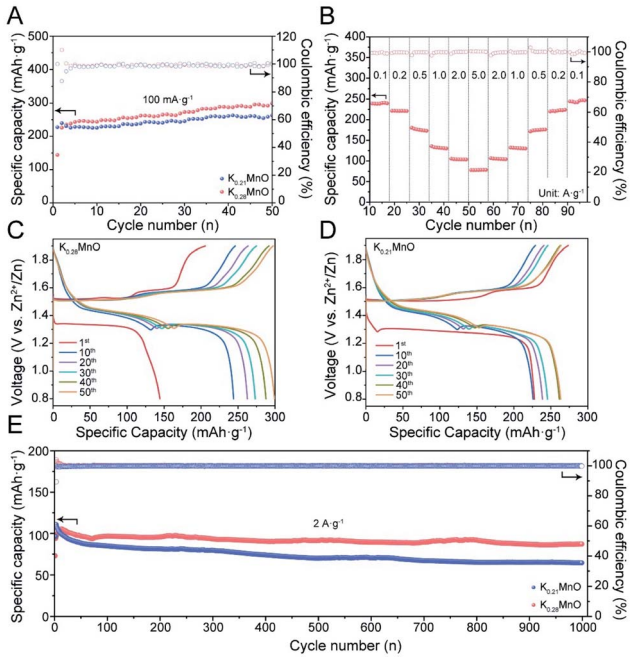

Fig. 3 Electrochemical performance of electrodes tested in coin cells. (A) Cycling performance of $K_{0.28}MO$ and $K_{0.21}MO$ materials at a current density of 100 mA g^{-1}. (B) Rate performance of $K_{0.28}MO$. (C and D) Charge/discharge profiles of $K_{0.28}MO$ and $K_{0.21}MO$ cells at 100 mA g^{-1}, respectively. (E) Cycling performance of $K_{0.28}MO$ and $K_{0.21}MO$ materials at a current density of 2 A g^{-1}.

Energy storage mechanism

To confirm the maintained structural integrity and explore the underlying energy storage mechanism of $K_{0.28}MO$, combined *ex situ* XRD, XPS, High Angle Annular Dark Field Scanning Transmission Electron Microscopy (HAADF-STEM), and NEXAFS measurements were carried out to determine if phase transitions of the pristine material and microstructural evolution are involved upon cycling. Fig. 4A provides the specific voltage points at which the coin cells were disassembled to obtain the cathodes for subsequent testing. As shown in Fig. 4B, the δ-MnO_2 phase with a characteristic peak at *ca.* 5.6° was observed throughout the cycling process, confirming that the primitive structure is retained upon cycling. This result contrasts with previous reports of phase transitions occurring after cycling.[29,32,56]

Also, as shown in Fig. 4B, a new phase with a strong characteristic diffraction peak (2θ) at 8° was discovered in the initial discharge process (A → B) and the later discharge process from 1.35 V to 0.8 V (E → F), which can be assigned to ZSH.[20] The change in O 1s XPS curves also reveals the emergence of S–O species at 532.8 eV and an enhanced peak at 531.9 eV corresponding to O–H species (Fig. 4C). The ZSH phase shows a unique two-dimensional layered structure formed by stacking of $Zn(OH)_2$ with $ZnSO_4$ from the electrolyte while absorbing water molecules between the layers. ZSH is formed on the surface of the cathode material (Fig. S14†). During both the initial charge process (B → C) and later charge process from 0.8 V to 1.55 V (F → G), the characteristic peaks of ZSH

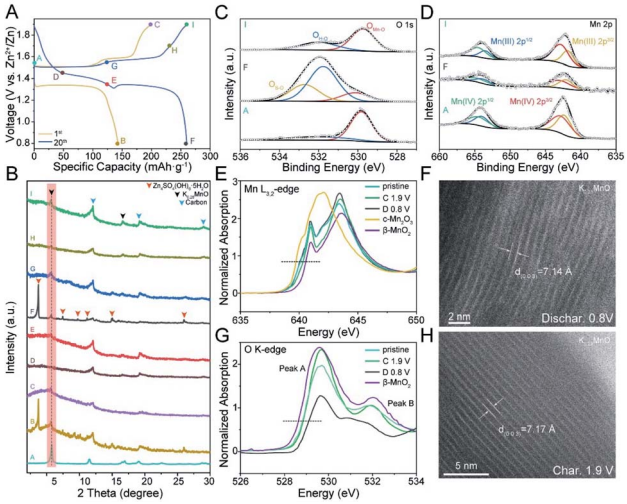

Fig. 4 Mechanism study of $K_{0.28}MO$ electrode. (A) Charge/discharge curves of $K_{0.28}MO$ at the 1st and 20th cycle. (B) *Ex situ* XRD pattern of rainsed cathode collected at various states marked in (A). (C and D) *Ex situ* XPS spectra of O 1s (C) and Mn 2p (D) at different discharge/charge states of the $K_{0.28}MO$ electrode. (E) *Ex situ* near-edge X-ray absorption fine structure (NEXAFS) spectra at Mn $L_{3,2}$-edge of pristine, charged, discharged $K_{0.28}MO$ and reference materials. (F) *Ex situ* High Angle Annular Dark Field Scanning Transmission Electron Microscopy (HAADF-STEM) image of $K_{0.28}MO$ at a fully discharged state. (G) *Ex situ* NEXAFS spectra at O K-edge of pristine, charged, discharged $K_{0.28}MO$ and reference materials. (H) *Ex situ* HAADF-STEM image of $K_{0.28}MO$ at a fully charged state.

disappear. With increasing discharge depth, the ZSH layers dissolve back to the electrode, indicating the reversible formation of the ZSH phase (Fig. S15†). The results confirm the reversible deposition/dissolution of the ZSH phase on the cathode material's surface.[20,23,57] It has been reported that based on the Zn^{2+}/H^+ intercalation mechanism in AZIBs, with the intercalation of H^+, OH^- is reversibly released to react with excessive Zn^{2+} and SO_4^{2-} in the electrolyte to deposit the ZSH layers.[23,57] Thus, the discovery of ZSH in this work confirms the dual ion intercalation mechanism for birnessite MnO_2 cathodes.

Considering the faster migration and smaller hydrated radius, the first discharge plateau shown in Fig. 4A is assigned as the intercalation of H^+. Due to the decrease of the H^+ around the cathodes and a further increase of the polarization, the intercalation of Zn^{2+} soon becomes dominant. The slower intercalation kinetics means that the intercalation of Zn^{2+} requires a higher overpotential, and thus the discharge plateau is lower.

The change of the Mn oxidation state on both surface and bulk structures was further studied. During the discharge process, the Mn(III) content increases while Mn(IV) content reduces; In the charging process, Mn(IV) content reaches a maximum value, indicating the highest oxidation state at fully charged state (Fig. 4D).

Reliable proof of the reversible change of the Mn oxidation state is provided by NEXAFS (Fig. 4E). Mn $L_{3,2}$-edge NEXAFS could directly probe the electron dipole-allowed transition from Mn 2p to unoccupied valence 3d states, strongly correlated with the electronic configuration and oxidation state. The systematic shift of L_3 leading edge position and gravity center of L_3/L_2 edge towards lower energies could indicate the decrease of average oxidation states. Compared to commercial β-MnO_2 and Mn_2O_3 electrodes, the average oxidation state at fully charged state is very close to Mn^{4+}, while at fully discharged state, the curve shows more resemblance with Mn_2O_3 with a negative energy shift (0.2 eV), indicating the presence of its lowest oxidation state (Mn^{3+}). The sharp absorption peaks at 641 eV at both charged and discharged states are distinguished from the main absorption edge, which is considered characteristic features of birnessite structure.[55]

Besides, as shown in Fig. 4G, the pre-edge feature in O K-edge NEXAFS spectra originates from electron transitions from ligand O 1s orbitals to unoccupied Mn 3d states due to the hybridization of O 2p and Mn 3d (t_{2g} and e_g) states. For Mn(IV) with $3d^3$ ($t_{2g}^3e_g^0$) configuration, two absorption peaks could be identified: the lower energy peak at 528.8 eV (Peak A) is attributed to spin-down t_{2g} and spin-up e_g transitions (nearly equivalent crystal field splitting and exchange splitting) and the higher energy peak at 532.0 eV (Peak B) arise from the spin-down e_g transitions. For Mn(III) with $3d^4$ ($t_{2g}^3e_g^1$) configuration, three absorption peaks could be observed: spin-up e_g, spin-down t_{2g} and spin-down e_g transitions, from low energies to high energies, respectively. As shown in Fig. 4G, for the charged state, the pre-edge feature is almost identical to β-MnO_2, while the discharged state presents a broad absorption peak (530.8 to 531.8 eV), which is contributed from Mn(III) content.

At the fully discharged state, the characteristic peak of $K_{0.28}MO$ slightly shifts towards higher angles, which can be ascribed to the intercalation of H^+/Zn^{2+} ions and enhanced ionic interaction. The corresponding (003) lattice spacing of $K_{0.28}MO$ at a full discharged state was observed as 7.14 Å (Fig. 4F), while the lattice spacing increased to 7.17 Å at full charged state, which is enlarged due to the deintercalation of H^+/Zn^{2+} and reduced ionic interaction (Fig. 4H).[49]

HAADF-STEM of $K_{0.28}MO$ is also applied to detect the orientation of (012) lattice plane. As shown in Fig. S16,† the lattice space remained stable during both the charge and discharge process. Moreover, the orientation of (012) lattice plane is disordered, which suggests possible lattice defects. Lattice defects provide pathways for ion intercalation/deintercalation, enabling higher capacity and fast ion diffusion kinetics.

Structural stabilization effect of K ions *via* DFT simulation

The structural details of MnO_2, therefore, deserve a more in-depth analysis. The rich polymorphic chemistry of MnO_2 comprises dense, tunnel and layered structures. The stable phase in the absence of intercalated cations is the rutile β-MnO_2, followed by the tunnel α-MnO_2 structure. The relative polymorph stability is modified by the presence and concentration of different cations,[6] with the α-MnO_2 phase becoming stable at low intercalation levels. Only at high intercalation does the layered birnessite δ-MnO_2 structure become the stable polymorph. Therefore, it is reasonable to expect a structural

strain upon electrochemical cycling in energy storage applications that varies the concentration of intercalated species.

The two materials investigated in the present work contain different amounts of pre-intercalated K, which may affect the phase stability; to understand whether this is the case, we have studied through DFT calculations the structure and stability of K_xMnO_2 in α and δ phases as a function of K content in the relevant range of $0 \leq x \leq 0.5$. Our calculations confirm that indeed the layered birnessite phase is unstable compared to α-MnO_2 in the absence of K. At low K content, up to $x = 0.125$, intercalation energy is higher in the tunnels of α-MnO_2 than in between the layers of δ-MnO_2 and the energy difference between the polymorphs increases (Fig. 5). However, further K intercalation above $x = 0.125$ is more stable in the δ-MnO_2 phase, where the 2-D layered structure provides a larger intercalation volume. At $x = 0.25$, all interstices of α-MnO_2 are fully occupied; the presence of any K above $x = 0.25$ requires split-interstitials in the tunnel α-MnO_2 phase, associated with strong destabilization energy, calculated as 3.7 eV per K ion. The difference in successive intercalation energies between alpha and delta is provided in Fig. S17.† Above *ca.* 0.26, the layered δ-MnO_2 polymorph becomes the thermodynamic ground state in the K_xMnO_2 chemistry. Enforcing an even higher K concentration of $x = 0.5$ in α-MnO_2 in the DFT calculations yields a layered structure resembling the δ phase upon geometry optimization (Fig. S17†), emphasizing the intercalation-induced structural instability. It is interesting to observe that the two materials studied experimentally have K content on opposite sides of the α–δ phase transition. The best performing $K_{0.28}MO$ has a K content that positions it in the phase space where the layered polymorph is stable, which substantiates the experimental observation of its phase stability upon cycling. In contrast, the $K_{0.21}MO$ material with lower K content will repeatedly cross the α–δ phase transition boundary upon further intercalation of Zn during cycling, explaining its structural instability.

In summary, the overall electrochemical reaction of $K_{0.28}MO$ can be illustrated as in Fig. 6A. The primitive birnessite phase is well maintained throughout the cycling process, while ZSH is deposited reversibly simultaneous H^+/Zn^{2+} intercalation/deintercalation, contributing to the overall capacity.

Commercialization potential

To further demonstrate the potential commercial applications of the as-designed materials, the battery was assembled with typical high mass loading used in commercial lithium-ion batteries (*ca.* 8–10 mg cm^{-2}). As shown in Fig. 6B, the AZIBs with high loading mass shows competent rate performance close to normal loading ones, which maintains *ca.* 200 mA h g^{-1} at 100 mA g^{-1} and keeps *ca.* 50 mA h g^{-1} at a high current density of 5 A g^{-1}. Besides, there is almost no capacity loss after stepwise current density changes. To compare with current commercial energy storage systems, a Ragone plot is constructed, and it is worth mentioning that the $K_{0.28}MO$ cell shows adequate energy and power densities, which indicates its potential for commercialization (Fig. 6C).

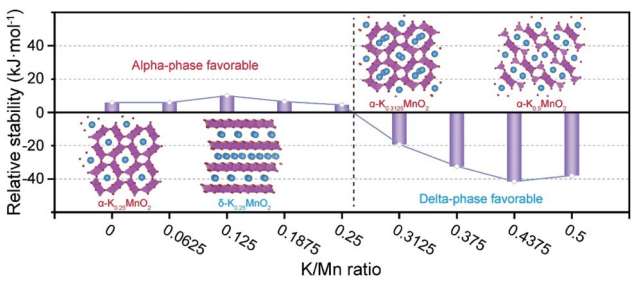

Fig. 5 The relative stability of delta phase to alpha phase as a function of K/Mn ratio *via* DFT simulation.

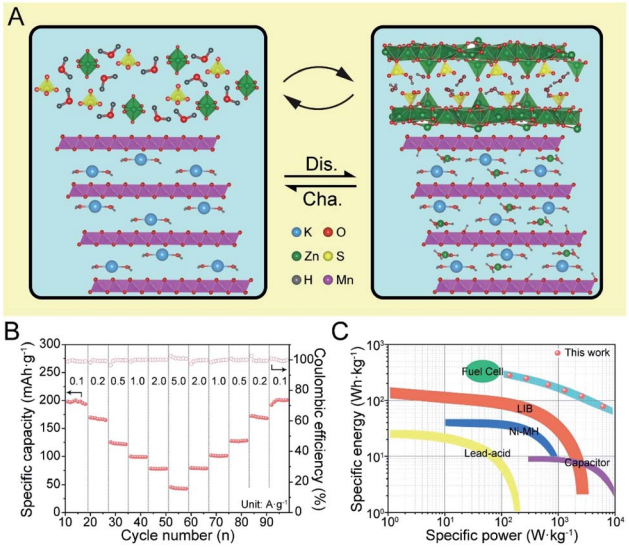

Fig. 6 Energy storage mechanism and potential for industrialization. (A) Schematic illustration of the electrochemical reaction of $K_{0.28}MO$ in aqueous AZIBs. (B) Rate performance of $K_{0.28}MO$ cell with high mass loading (*ca.* 10 mg cm^{-2}). (C) Comparison of the Ragone plot (based on the weight of cathode materials) of the $K_{0.28}MO$ cell with typical commercial energy storage systems.

Conclusions

In summary, the relationship between phase stability, structural integrity and the proportion of pre-intercalated ions was established for K pre-intercalated MnO_2 cathodes. The underlying mechanisms responsible for the phase instability of pristine birnessite MnO_2 upon cycling are identified through a combined experimental and computational approach. K concentration above a threshold value, as realized in $K_{0.28}MO$, is critical for phase stability. Zn intercalation in $K_{0.28}MO$ has been characterized and quantified under different electrochemical conditions. We further demonstrated that Zn–$K_{0.28}MO$ cells achieved a high capacity of 300 mA h g^{-1} and long-term cycle life of up to 1000 cycles without any significant decrease in the specific capacity. The enhanced rate performance also confirmed the fast kinetics enabled by K^+ supported pathways. These findings signal reasonable potential and stimulate future research *via* intercalation engineering for improving the performance of AZIBs.

Conflicts of interest

The authors declare no conflict of interest.

Acknowledgements

The authors acknowledge Diamond Light Source and electron Physical Science Imaging Centre for the allocated beamtime at E01 (session ID: MG24450). The authors acknowledge Helmholtz-Zentrum Berlin for the allocated beamtime at the ISISS beamline of BESSY II (proposal ID: 19108389-ST). The authors would like to thank the Engineering and Physical Sciences Research Council (EPSRC, EP/L015862/1, EP/R023581/1), STFC Batteries Network (ST/R006873/1), RSC Mobility Grant (M19-7656) for funding support. *Via* the authors' membership of the UK's HEC Materials Chemistry Consortium funded by EPSRC (EP/L000202), this work used the ARCHER UK National Supercomputing Service (http://www.archer.ac.uk). The authors are grateful to the UK Materials and Molecular Modelling Hub for computational resources, partially funded by EPSRC (EP/P0202194/1). The authors acknowledge the use of the UCL Kathleen High Performance Computing Facility (Kathleen@UCL) and associated support services to complete this work. Y. Jiao thanks the funding support from China Scholarship Council/University College London for the joint PhD scholarship. Y. J. thanks the support from his colleagues and families. In particular, Y. J. wants to thank H. X. for her invaluable support and encouragement over the years. Will you marry me?

Notes and references

1 M. Pasta, C. D. Wessells, R. A. Huggins and Y. Cui, *Nat. Commun.*, 2012, **3**, 1149.
2 Y.-K. Sun, S.-T. Myung, B.-C. Park, J. Prakash, I. Belharouak and K. Amine, *Nat. Mater.*, 2009, **8**, 320.
3 M. Armand, *Nature*, 2001, **414**, 359–367.
4 J. Hassoun, K.-S. Lee, Y.-K. Sun and B. Scrosati, *J. Am. Chem. Soc.*, 2011, **133**, 3139–3143.
5 N. Nitta, F. Wu, J. T. Lee and G. Yushin, *Mater. Today*, 2015, **18**, 252–264.
6 J.-M. Tarascon and M. Armand, in *Materials for Sustainable Energy: A Collection of Peer-Reviewed Research and Review Articles from Nature Publishing Group*, World Scientific, 2011, pp. 171–179.
7 Z. Liu, J. Wang, H. Ding, S. Chen, X. Yu and B. Lu, *ACS Nano*, 2018, **12**, 8456–8466.
8 A. Ponrouch, C. Frontera, F. Bardé and M. R. Palacín, *Nat. Mater.*, 2016, **15**, 169–172.
9 K. Share, A. P. Cohn, R. Carter, B. Rogers and C. L. Pint, *ACS Nano*, 2016, **10**, 9738–9744.
10 L. Ma, N. Li, C. Long, B. Dong, D. Fang, Z. Liu, Y. Zhao, X. Li, J. Fan and S. Chen, *Adv. Funct. Mater.*, 2019, **29**, 1906142.
11 F. Wan and Z. Q. Niu, *Angew. Chem., Int. Ed.*, 2019, **58**, 16358–16367.
12 F. Wan, X. Y. Wang, S. S. Bi, Z. Q. Niu and J. Chen, *Sci. China: Chem.*, 2019, **62**, 609–615.
13 Y. Liu, P. Hu, H. Liu, X. Wu and C. Zhi, *Materials Today Energy*, 2020, **17**, 100431.
14 S. Liu, H. Zhu, B. Zhang, G. Li, H. Zhu, Y. Ren, H. Geng, Y. Yang, Q. Liu and C. C. Li, *Adv. Mater.*, 2020, **32**, 2001113.
15 K. Lu, B. Song, Y. X. Zhang, H. Y. Ma and J. T. Zhang, *J. Mater. Chem. A*, 2017, **5**, 23628–23633.
16 L. Y. Zhang, L. Chen, X. F. Zhou and Z. P. Liu, *Sci. Rep.*, 2015, **5**, 18263.
17 M. Tian, C. Liu, J. Zheng, X. Jia, E. P. Jahrman, G. T. Seidler, D. Long, M. Atif, M. Alsalhi and G. Cao, *Energy Storage Materials*, 2020, **29**, 9–16.
18 L. Ma, S. Chen, C. Long, X. Li, Y. Zhao, Z. Liu, Z. Huang, B. Dong, J. A. Zapien and C. Zhi, *Adv. Energy Mater.*, 2019, **9**, 1902446.
19 Z. Chen, P. Wang, Z. Ji, H. Wang, J. Liu, J. Wang, M. Hu and Y. Huang, *Nano-Micro Lett.*, 2020, **12**, 75.
20 G. Fang, C. Zhu, M. Chen, J. Zhou, B. Tang, X. Cao, X. Zheng, A. Pan and S. Liang, *Adv. Funct. Mater.*, 2019, **29**, 1808375.
21 J. H. Huang, Z. Wang, M. Y. Hou, X. L. Dong, Y. Liu, Y. G. Wang and Y. Y. Xia, *Nat. Commun.*, 2018, **9**, 2906.
22 S. Khamsanga, R. Pornprasertsuk, T. Yonezawa, A. A. Mohamad and S. Kheawhom, *Sci. Rep.*, 2019, **9**, 8441.
23 J. J. Wang, J. G. Wang, H. Y. Liu, C. G. Wei and F. Y. Kang, *J. Mater. Chem. A*, 2019, **7**, 13727–13735.
24 T. Xiong, Z. G. Yu, H. Wu, Y. Du, Q. Xie, J. Chen, Y. W. Zhang, S. J. Pennycook, W. S. V. Lee and J. Xue, *Adv. Energy Mater.*, 2019, **9**, 1803815.
25 L. E. Blanc, D. Kundu and L. F. Nazar, *Joule*, 2020, **4**, 771–799.
26 M. Song, H. Tan, D. Chao and H. J. Fan, *Adv. Funct. Mater.*, 2018, **28**, 1802564.
27 B. Tang, L. Shan, S. Liang and J. Zhou, *Energy Environ. Sci.*, 2019, **12**, 3288–3304.
28 M. H. Alfaruqi, J. Gim, S. Kim, J. Song, D. T. Pham, J. Jo, Z. Xiu, V. Mathew and J. Kim, *Electrochem. Commun.*, 2015, **60**, 121–125.
29 S.-D. Han, S. Kim, D. Li, V. Petkov, H. D. Yoo, P. J. Phillips, H. Wang, J. J. Kim, K. L. More and B. Key, *Chem. Mater.*, 2017, **29**, 4874–4884.
30 B. Lee, H. R. Lee, H. Kim, K. Y. Chung, B. W. Cho and S. H. Oh, *ChemComm*, 2015, **51**, 9265–9268.
31 B. Lee, C. S. Yoon, H. R. Lee, K. Y. Chung, B. W. Cho and S. H. Oh, *Sci. Rep.*, 2014, **4**, 6066.
32 X. W. Wu, Y. H. Xiang, Q. J. Peng, X. S. Wu, Y. H. Li, F. Tang, R. C. Song, Z. X. Liu, Z. Q. He and X. M. Wu, *J. Mater. Chem. A*, 2017, **5**, 17990–17997.
33 N. Zhang, F. Cheng, J. Liu, L. Wang, X. Long, X. Liu, F. Li and J. Chen, *Nat. Commun.*, 2017, **8**, 405.
34 C. Y. Zhu, G. Z. Fang, J. Zhou, J. H. Guo, Z. Q. Wang, C. Wang, J. Y. Li, Y. Tang and S. Q. Liang, *J. Mater. Chem. A*, 2018, **6**, 9677–9683.
35 H. Pan, Y. Shao, P. Yan, Y. Cheng, K. S. Han, Z. Nie, C. Wang, J. Yang, X. Li and P. Bhattacharya, *Nat. Energy*, 2016, **1**, 16039.
36 M. Chamoun, W. R. Brant, C.-W. Tai, G. Karlsson and D. Noréus, *Energy Storage Materials*, 2018, **15**, 351–360.

37 M. H. Alfaruqi, V. Mathew, J. Song, S. Kim, S. Islam, D. T. Pham, J. Jo, S. Kim, J. P. Baboo, Z. Xiu, K. S. Lee, Y. K. Sun and J. Kim, *Chem. Mater.*, 2017, **29**, 1684–1694.
38 J. Li, K. McColl, X. Lu, S. Sathasivam, H. Dong, L. Kang, Z. Li, S. Zhao, R. Wang, D. J. L. Brett, P. R. Shering, F. Cora, G. He, A. Kafizas, C. J. Carmalt and I. P. Parkin, *Adv. Energy Mater.*, 2020, **10**, 2000058.
39 F. W. Ming, H. F. Liang, Y. J. Lei, S. Kandambeth, M. Eddaoudi and H. N. Alshareef, *ACS Energy Lett.*, 2018, **3**, 2602–2609.
40 B. Wu, G. Zhang, M. Yan, T. Xiong, P. He, L. He, X. Xu and L. Mai, *Small*, 2018, **14**, 1703850.
41 Y. X. Zeng, X. Y. Zhang, R. F. Qin, X. Q. Liu, P. P. Fang, D. Z. Zheng, Y. X. Tong and X. H. Lu, *Adv. Mater.*, 2019, **31**, 1903675.
42 Q. C. Zhang, C. W. Li, Q. L. Li, Z. H. Pan, J. Sun, Z. Y. Zhou, B. He, P. Man, L. Y. Xie, L. X. Kang, X. N. Wang, J. Yang, T. Zhang, P. P. Shum, Q. W. Li, Y. G. Yao and L. Wei, *Nano Lett.*, 2019, **19**, 4035–4042.
43 N. Zhang, F. Cheng, Y. Liu, Q. Zhao, K. Lei, C. Chen, X. Liu and J. Chen, *J. Am. Chem. Soc.*, 2016, **138**, 12894–12901.
44 X. Deng, Y. Xu, Q. An, F. Xiong, S. Tan, L. Wu and L. Mai, *J. Mater. Chem. A*, 2019, **7**, 10644–10650.
45 P. He, G. B. Zhang, X. B. Liao, M. Y. Yan, X. Xu, Q. Y. An, J. Liu and L. Q. Mai, *Adv. Energy Mater.*, 2018, **8**, 1702463.
46 M. Yan, P. He, Y. Chen, S. Wang, Q. Wei, K. Zhao, X. Xu, Q. An, Y. Shuang and Y. Shao, *Adv. Mater.*, 2018, **30**, 1703725.
47 X. Yao, Y. Zhao, F. A. Castro and L. Mai, *ACS Energy Lett.*, 2019, **4**, 771–778.
48 T. Sun, Q. Nian, S. Zheng, J. Shi and Z. Tao, *Small*, 2020, **16**, 2000597.
49 J. Xiao, L. Wan, X. Wang, Q. Kuang, S. Dong, F. Xiao and S. Wang, *J. Mater. Chem. A*, 2014, **2**, 3794–3800.
50 H. He, H. Tong, X. Song, X. Song and J. Liu, *J. Mater. Chem. A*, 2020, **8**, 7836–7846.
51 Z. Hou, M. Dong, Y. Xiong, X. Zhang, H. Ao, M. Liu, Y. Zhu and Y. Qian, *Small*, 2020, **16**, 2001228.
52 O. Ghodbane, F. Ataherian, N. L. Wu and F. Favier, *J. Power Sources*, 2012, **206**, 454–462.
53 Y. Yang, X. Su, L. Zhang, P. Kerns, L. Achola, V. Hayes, R. Quardokus, S. L. Suib and J. He, *ChemCatChem*, 2019, **11**, 1689.
54 C. Zhan, J. Lu, A. J. Kropf, T. Wu, A. N. Jansen, Y.-K. Sun, X. Qiu and K. Amine, *Nat. Commun.*, 2013, **4**, 2437.
55 R. Qiao, T. Chin, S. J. Harris, S. Yan and W. Yang, *Current Applied Physics*, 2013, **13**, 544–548.
56 M. H. Alfaruqi, S. Islam, D. Y. Putro, V. Mathew, S. Kim, J. Jo, S. Kim, Y. K. Sun, K. Kim and J. Kim, *Electrochim. Acta*, 2018, **276**, 1–11.
57 L. Chen, Z. Yang, H. Qin, X. Zeng and J. Meng, *J. Power Sources*, 2019, **425**, 162–169.